Wet-Chemical Synthesis of ZnFe$_2$O$_4$ MNPs by Sol-gel Auto-Combustion Method, Structural, Magnetic, and DC-Electrical Characterizations

Ram S. Barkule[1], Santosh D. More[2], Balwan U. Patil[3]

Department of Physics, Sundarrao More Arts, Commerce and Science College, Poladpur, Raigad, India[1]

Department of Physics, Deogiri College, Chhatrapati Sambhajinagar, India[2]

Department of Physics, Kohinoor Arts, Commerce and Science College, Chhatrapati Sambhajinagar, India[3]

Abstract: *ZnFe$_2$O$_4$ magnetic nanoparticles (MNPs) were successfully synthesized using the sol-gel auto-combustion method, with citric acid (C$_2$H$_2$O$_2$) employed as the fuel. X-ray diffraction (XRD) analysis confirmed the formation of a cubic spinel structure with the Fd3m-Oh7 space group, and the lattice constant (a) was measured to be 8.384 ± 0.05 Å. Debye-Scherrer's method for analyzing peak broadening revealed an average crystallite size of 36 nm. Fourier-transform infrared (FT-IR) spectroscopy identified two key metal-oxide bands at approximately 541 cm^{-1} (O-M Oct) and 409 cm^{-1} (O-M Td), which correspond to the metal-oxygen bonds at the octahedral and tetrahedral sites, respectively, thereby validating the structural integrity of the synthesized material. Magnetic characterization showed a saturation magnetization (Ms) of ~50 emu/g, a remanent magnetization (Mr) of ~17 emu/g, and a magneton number (nB) of 1.77 emu/g. The activation energy (Ea) was calculated to be 3.11 eV. Furthermore, DC electrical resistivity measurements, consistent with the Arrhenius equation, confirmed the semiconducting nature of the ZnFe$_2$O$_4$ MNPs.*

Keywords: ZnFe$_2$O$_4$ MNPs, Sol-gel synthesis, Infra-Red spectroscopy, DC-Electrical property.

I. INTRODUCTION

Various techniques are widely employed across multiple industries for research and development, playing a pivotal role in advancing technologies in sectors such as medical devices, pharmaceuticals, food processing, agriculture, pollution control, materials science, security systems, and aerospace communication [1-3]. These techniques have become essential tools for tailoring the physical and chemical properties of nanoparticles, making them suitable for a variety of commercial applications. Different techniques can modify the internal structure and surface characteristics of nanoparticles, which in turn influences their structural and magnetic properties. The ability to customize these properties is particularly valuable in fields such as electronics, catalysis, and biomedical applications, where precise control over material behavior is crucial [4]. Spinel ferrites, represented by the general formula MeFe$_2$O$_4$ (where Me can be divalent cations such as Fe^{2+}, Co^{2+}, Ni^{2+}, Cu^{2+}, Mg^{2+}, or Zn^{2+}), have garnered significant attention from researchers due to their unique combination of electromagnetic properties, chemical stability, mechanical strength, and tunable magnetic characteristics [5]. Specifically, zinc ferrite (ZnFe$_2$O$_4$) nanoparticles (NPs) have become a subject of intensive study because of their high electromagnetic performance, low coercivity, moderate saturation magnetization, and excellent stability [6]. These attributes make ZnFe$_2$O$_4$ NPs ideal candidates for a wide range of technological applications, including the development of soft magnets, low-loss materials for high-frequency applications, gas sensors, semiconductor photocatalysts, and energy conversion devices such as magnetocaloric pumps [7, 8]. Recent research has demonstrated the promising potential of ZnFe$_2$O$_4$ nanoparticles in gas-sensing applications. Studies have shown that ZnFe$_2$O$_4$ NPs are sensitive to gases such as methane (CH$_4$), hydrogen sulfide (H$_2$S), liquefied petroleum gas (LPG), and ethanol (C$_2$H$_5$OH), making them valuable for environmental monitoring and industrial gas detection systems. These findings highlight the versatility and functional adaptability of ZnFe$_2$O$_4$ NPs, further enhancing their appeal in both scientific research and industrial applications. In this study, ZnFe$_2$O$_4$ nanoparticles were synthesized using the sol-gel auto-combustion technique, a method widely recognized for its simplicity, cost-effectiveness, and

ability to produce nanoparticles with excellent chemical homogeneity and physical uniformity [9]. The sol-gel process is particularly advantageous over other synthesis methods due to its capacity for ideal molecular mixing of starting materials, which leads to the formation of highly uniform nanoparticles with controlled size and morphology. The synthesis of $ZnFe_2O_4$ NPs through sol-gel auto-combustion ensures that the resulting particles exhibit a high degree of purity and structural integrity, making them suitable for various advanced technological applications [10]. Enhancing our understanding of how the sol-gel synthesis method affects the magnetic properties of the nanoparticles. This comprehensive study offers significant contributions to the field of materials science by providing a deeper understanding of the sol-gel synthesis process, the structural and magnetic characterization of $ZnFe_2O_4$ nanoparticles, and the potential for tuning these properties for various applications. The ability to control and optimize the physical properties of $ZnFe_2O_4$ NPs through sol-gel synthesis and subsequent characterization techniques holds promise for the development of advanced materials with tailored functionalities. Such materials could play a crucial role in emerging technologies, including magnetic data storage, catalysis, gas sensing, and biomedical applications. Through ongoing research, further improvements in the synthesis and characterization of spinel ferrites like $ZnFe_2O_4$ are expected, paving the way for their widespread use in cutting-edge technologies [11, 12].

II. EXPERIMENTAL

Materials

Fisher Scientific Pvt Ltd provided AR-grade (Analytical Reagent grade) chemicals for the synthesis process, ensuring precision, consistency, and reliability in the experimental outcomes. These ultrafine analytical reagents, with a remarkable purity of 99.9%, were specifically selected to meet the rigorous demands of advanced laboratory instruments used in cutting-edge research. The chemicals used in the experiment included ferrous nitrate $(Fe(NO_3)_3 \cdot 9H_2O)$, zinc nitrate $(Zn(NO_3)_2 \cdot 6H_2O)$, citric acid $(C_6H_8O_7)$, ammonia solution (NaOH), and deionized water, each playing a crucial role in the synthesis process. Ferrous nitrate served as the primary source of iron ions, zinc nitrate introduced zinc ions, and citric acid acted as a chelating agent, ensuring uniform mixing of the metal ions by forming metal-citrate complexes. Ammonia solution was employed to adjust the pH level, facilitating the precipitation of metal hydroxides, while deionized water, used as a solvent, ensured no impurities interfered with the reactions. The chemicals, used without further purification, were ideal for maintaining the integrity of the synthesis process, ensuring reproducibility and accuracy in the results. This careful selection of high-purity reagents minimized the risk of contamination or unwanted side reactions that could alter the properties of the synthesized material. The meticulous handling and precise proportioning of each chemical during the experimental procedure were critical for controlling key material properties, such as crystallite size, phase purity, and magnetic behavior. By adhering to these high standards, the experiment successfully met the stringent requirements necessary for producing reliable and scientifically valuable data, highlighting the importance of chemical quality and experimental rigor in research.

III. SYNTHESIS OF $ZNFE_2O_4$ MNPS

$ZnFe_2O_4$ nanoparticles were successfully synthesized using the sol-gel auto-combustion method, utilizing stoichiometric proportions of AR-grade ferric nitrate $(Fe(NO_3)_3 \cdot 9H_2O)$ and zinc nitrate $(Zn(NO_3)_2)$ with a purity of 99.9%. The metal ions, produced by dissolving the transition metal starting materials in deionized water, were complexed with citric acid $(C_6H_8O_7)$ in a molar ratio of 1:3, forming the precursor for ferrite ceramics. The formation of coordinate bonds between electron-deficient metal atoms and the electron-rich ions of citric acid was crucial in driving the sol-gel process. The pH of the solution was carefully maintained at 7 by adding ammonia solution (NH_3) drop by drop, as experiments indicated that the pH significantly influenced the formation of the precursor's network structure and the combustion behavior during thermally induced auto-catalytic redox reactions. Maintaining the optimal pH also contributed to the porous nature of the precursor, which is essential for the auto-combustion process. The mixed metal nitrate aqueous solution was continuously stirred and heated on a hotplate magnetic stirrer at a temperature of 70–80°C. During the evaporation process, the solution gradually transformed into a dried gel, a critical step in the auto-catalytic combustion process. Upon further heating, the nitrate solution turned viscous and brown, eventually forming a sticky brown gel. This gel began to bubble and spontaneously ignited, burning completely with a glowing flint, resulting in a fluffy, loose powder of pre-sintered zinc ferrite. The exothermic redox reaction between the oxidant

IJARSCT

ISSN (Online) 2581-9429

International Journal of Advanced Research in Science, Communication and Technology (IJARSCT)

International Open-Access, Double-Blind, Peer-Reviewed, Refereed, Multidisciplinary Online Journal

Impact Factor: 7.53

Volume 4, Issue 1, September 2024

and reductant produced a ferrite-phased, ash-like material, which was then dried and gently ground. After thermogravimetric analysis, the sample was annealed at 600°C for 12 hours in a programmable furnace with a heating rate of 5°C per minute, followed by cooling at room temperature at the same rate. This annealing step controlled the crystallinity, particle aggregation, and formation of ferrite phases while minimizing impurity phases. The post-annealed powder was further ground using a simple mortar and pestle in dry conditions, providing an eco-friendly approach. Finally, disc-shaped pellets (10 mm in diameter and 3 mm in height) were formed by applying a pressure of 5 tons/cm² for 5 minutes using a hydraulic press.
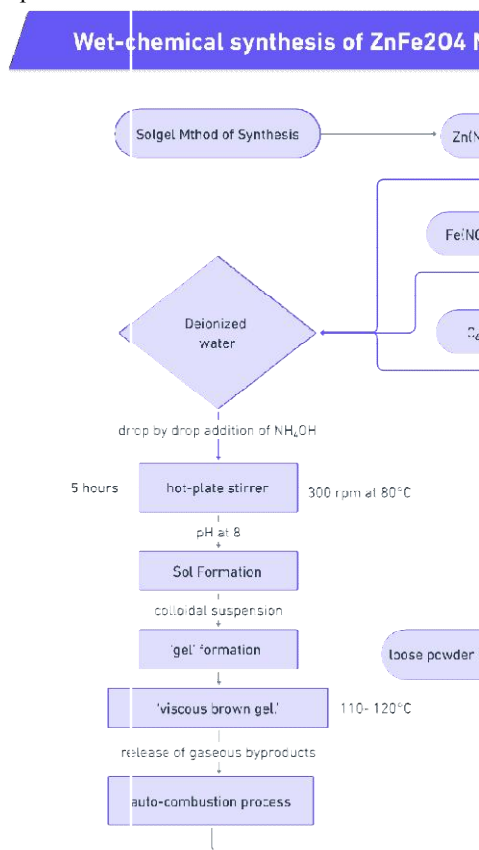
Figure 1 schematic overview of sol-gel auto-combustion synthesis process of $ZnFe_2O_4$ MNPs.

IV. CHARACTERIZATIONS TECHNIQUES

The crystal phase of the synthesized $ZnFe_2O_4$ magnetic nanoparticles (MNPs) was determined using X-ray diffraction (XRD), a crucial technique for identifying the crystallographic structure and phase composition of materials. XRD measurements were conducted at room temperature, specifically within the range of 28–33°C, to avoid thermal effects that could interfere with structural analysis. A Bruker D-8 X-ray diffractometer, operating under precise conditions of 45 kV and 30 mA, was used to generate high-intensity X-rays. The diffractometer scanned the sample over a diffraction angle range (2θ) of 20°–80°, providing detailed information about the crystal planes and lattice parameters of the material. The X-ray source utilized was Cu-Kα radiation with a wavelength of 1.54439 Å, which is standard in XRD studies due to its effective penetration and interaction with the sample, resulting in clear diffraction peaks. These peaks were analyzed to confirm the formation of the $ZnFe_2O_4$ spinel structure and to detect any secondary phases or impurities that may have arisen during synthesis. In addition to XRD, Fourier transform infrared (FT-IR) spectroscopy was employed to further characterize the chemical bonding and functional groups present in the $ZnFe_2O_4$ MNPs. FT-IR is a powerful technique for analyzing molecular vibrational modes and provides insights into the chemical structure. The FT-IR spectra were recorded over a range of 4000–300 cm⁻¹, allowing for the detection of various functional

groups, such as metal-oxygen (M-O) bonds, which are characteristic of ferrite materials. Specific absorption bands corresponding to metal-nitrate interactions, metal-oxygen stretching vibrations, and organic residues from the sol-gel process were identified, offering a comprehensive understanding of the sample's molecular composition. The magnetic properties of the synthesized $ZnFe_2O_4$ MNPs were examined using a pulse-field hysteresis loop, measured with a loop tracer device at room temperature. This hysteresis loop is critical for evaluating the magnetic behavior of materials, providing data on parameters such as coercivity, remanence, and saturation magnetization. These parameters are essential for understanding the magnetic response of the $ZnFe_2O_4$ MNPs and their potential applications in areas like magnetic storage, sensors, and biomedical fields. The unique magnetic characteristics, resulting from the sol-gel synthesis method and the precise composition of zinc, zinc, and iron, were assessed to determine their performance and utility in various technological applications. To evaluate the electrical properties of the $ZnFe_2O_4$ MNPs, DC-electrical resistivity measurements were performed. This is important for determining the material's suitability for electronic and magnetic devices. The resistivity measurements were carried out using a two-probe method on a pelletized sample. The pellet, with a diameter of 10 mm and a thickness of 2 mm, was compressed to ensure accurate resistivity readings and simulate conditions encountered in real-world applications. Copper electrodes were placed in contact with the sample to measure the voltage drop, while a Keithley model 614 digital electrometer recorded the resistivity values. This setup provided reliable data on the sample's electrical resistivity, offering insights into how the material's microstructure and composition affect its electrical conductivity. The combined use of XRD, FT-IR spectroscopy, pulse-field hysteresis, and electrical resistivity measurements provided a thorough characterization of the $ZnFe_2O_4$ MNPs. Each technique contributed valuable insights into the structural, chemical, magnetic, and electrical properties of the material, which are crucial for its potential applications in technology and science. The results of these analyses confirmed the successful synthesis of high-quality $ZnFe_2O_4$ MNPs, validated the sol-gel auto-combustion method used, and laid the groundwork for further exploration of this material in advanced applications.

V. RESULTS AND DISCUSSION

X-ray diffraction of $ZnFe_2O_4$ MNPs

The X-ray diffraction (XRD) patterns of $ZnFe_2O_4$ nanoparticles (MNPs), both before and after exposure to 100 kGy of gamma irradiation, were recorded using a Model X'PertPRO MPD PANalytical at room temperature. The XRD analysis was conducted over a 2θ range of 20° to 80°, utilizing Cu-Kα radiation ($\lambda = 1.5405$ Å) with a step size of 0.02° and a counting time of 1 second per step, resulting in a total acquisition time of 3 hours. The resulting Bragg reflections were compared with JCPDS card number 22-1012 to identify the crystalline phases present. The XRD pattern confirmed the presence of a single-phase $ZnFe_2O_4$ with a face-centered cubic spinel structure. X-ray diffractometry is a key technique for assessing and distinguishing between size-induced and strain-induced broadening of XRD peaks. The broadening can be analyzed through Lorentzian and Gaussian profiles of the typical XRD peaks, such as (220) and (440) [13].

Figure 2 presents the X-ray diffraction (XRD) pattern of $ZnFe_2O_4$ magnetic nanoparticles (MNPs) synthesized via the sol-gel auto-combustion method at room temperature, covering a (2θ) range of 20°–80°.
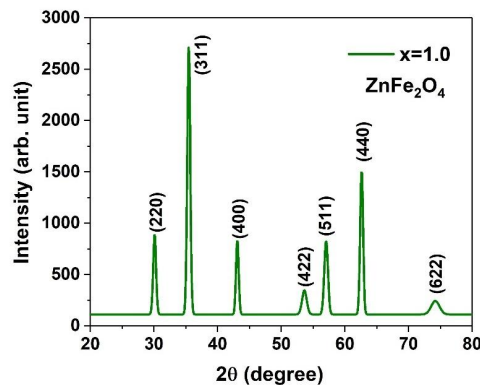
Figure 2 X-ray diffraction (XRD) pattern of $ZnFe_2O_4$ MNPs

The X-ray diffraction (XRD) pattern presented corresponds to $ZnFe_2O_4$ MNPs, indicating the successful synthesis of zinc ferrite with a cubic spinel structure. The sharp and distinct diffraction peaks, indexed with Miller indices such as (311), (220), (400), (422), (511), (440), and (622) [14, 15], suggest a highly crystalline material with well-defined structural order. The most intense peak, corresponding to the (311) plane, is characteristic of spinel ferrites. Additionally, the absence of any extra peaks indicates that the sample is phase pure, without detectable impurities. Overall, the pattern confirms the formation of a highly crystalline, single-phase zinc ferrite [16].

Table 1. Miller indices (hkl), Bragg's angle (θ), Interplanar spacing (d), lattice constant (a) of $ZnFe_2O_4$ MNPs.

h	k	l	2θ	θ	Sinθ	2Sinθ	d	(a/d)^2	a
2	2	0	30.105	15.053	0.260	0.519	2.965	7.987	8.387
3	1	1	35.466	17.733	0.305	0.609	2.528	10.985	8.386
4	0	0	43.100	21.550	0.367	0.735	2.097	15.976	8.386
4	2	2	53.634	26.817	0.451	0.902	1.707	24.100	8.363
5	1	1	57.049	28.524	0.478	0.955	1.613	27.002	8.380
4	4	0	62.627	31.313	0.520	1.040	1.482	31.983	8.382
6	2	2	74.205	37.102	0.603	1.207	1.277	43.088	8.468
									8.393

The provided table outlines the Miller indices and corresponding diffraction parameters for zinc ferrite $ZnFe_2O_4$ MNPs confirming the material's cubic spinel structure [17]. The 2θ values, ranging from 30° to 74°, align with typical XRD patterns for spinel ferrites. The interplanar spacing d-spacing decreases with increasing diffraction angles, with the largest spacing (2.965 Å) for the (220) plane and the smallest (1.277 Å) for the (622) plane, consistent with higher Miller indices. phase values match well with expected results for zinc ferrite, indicating a well-crystallized, phase-pure material [18]. Importantly, no impurity peaks were observed in the diffraction pattern, indicating the purity of the synthesized sample. Structural properties such as lattice constant (a), crystallite size (t), bulk density (dB), X-ray density (dX), and porosity (P) are listed in **Table 1**, with the lattice parameter calculated using the appropriate formula. [19] $a = d_{hkl} \sqrt{h^2 + k^2 + l^2}$; Where (d) represents the interplanar distance of two planes, (a) represents the lattice constant, and (hkl) represents the miller indices of each plane in the plane family. The lattice parameter value of $ZnFe_2O_4$ MNPs was determined by Debye- Scherrer formula [20, 21],

$$D = \frac{k\lambda}{\beta \cos\theta} \tag{1}$$

Where k is the constant with the value of 0.89, is the wavelength of the X-ray light source (1.540), is the full width at half maximum (FWHM), and is the glancing angle. The lattice constant (a) values showed consistency across different planes, with minor variations, averaging around 8.393 Å. This confirms the formation of a well-structured cubic spinel crystal with minimal distortions. These findings suggest that the nanoparticles were synthesized with high crystalline quality, in line with the expected properties of ferrite materials. The observed decrease in (d)-spacing with increasing Bragg's angle follows standard crystallographic behavior, affirming the accuracy of the measurements and the integrity of the synthesized material [22]. Based on this relationship, the X-ray density (d_X) of the $ZnFe_2O_4$ MNPs was calculated to be 5.47 g/cm³ [23]; $d_x = \frac{8M}{N_A a^3}$, Where dx is the X-ray density and M is the composition's relative molecular weight. The multiplication factor 8 was utilised as there are 8 formula units in a unit cell. N_A is the Avogadro's number, while (a) is the lattice constant. The Archimedes principle was used to compute the bulk density d_B of samples. Zinc ferrite's predicted bulk density was found to be 4.246 gm/cm^3. The distances between magnetic ions (hopping lengths) L_A and L_B at the tetrahedral (A)-site and octahedral (B)-site were estimated using the corresponding relations [24, 25].

$$L_A = \frac{a\sqrt{3}}{4} \tag{2}$$

$$L_B = \frac{a\sqrt{2}}{4} \tag{3}$$

Table 2 hopping lengths L_A and L_B, d_{AX}, d_{BX}, d_{AXE}, d_{BXE}, d_{BXEu}, and r_A, r_B for $ZnFe_2O_4$ MNPs

ZnFe$_2$O$_4$ nanoparticles (MNPs)									
(a) Å	**L_A**	**L_B**	**d_{AX}**	**d_{BX}**	**d_{AXE}**	**d_{BXE}**	**d_{BXEu}**	**r_A**	**r_B**
8.393	2.531	2.452	1.904	2.049	3.110	2.825	2.969	0.584	0.728

FT-IR analysis of ZnFe$_2$O$_4$ MNPs

The FTIR spectrum of $ZnFe_2O_4$ magnetic nanoparticles (MNPs) at room temperature (RT) was measured over a wide wavenumber range of 350–4000 cm^{-1}, as shown in **Figure 3**. This range is crucial for identifying the different vibrational modes within the material. In the FTIR spectra of spinel ferrites, two distinct absorption peaks are typically observed in the region between 370 and 600 cm^{-1}, corresponding to the metal-oxygen (M-O) stretching vibrations [26]. These peaks are of particular significance, as they represent the unique vibrational "fingerprint" of spinel ferrites and help characterize the crystal structure and bonding environment within the material. For $ZnFe_2O_4$ MNPs, the higher wavenumber absorption band at 541 cm^{-1} (v_1) is attributed to the metal-oxygen stretching vibrations at the tetrahedral (A) site of the spinel lattice. This site is characterized by a stronger bond due to the shorter distance between the oxygen and metal ions (specifically iron in this case). The lower wavenumber band at 409 cm^{-1} (v_2), on the other hand, corresponds to the metal-oxygen stretching vibrations at the octahedral [B] site, where the oxygen-iron bond is slightly longer [27, 28].
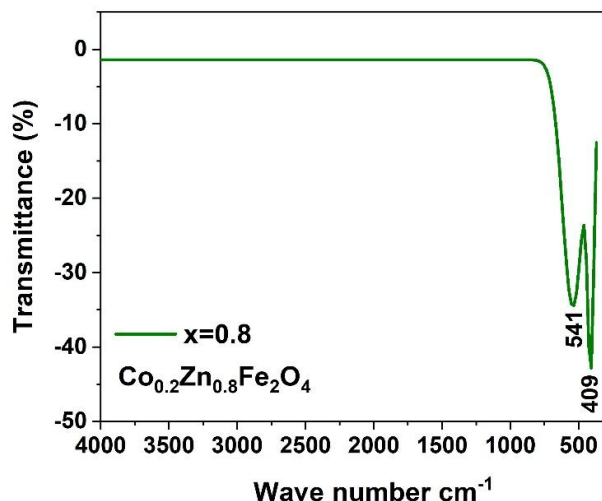

Figure 3 FTIR spectra of ZnFe$_2$O$_4$ MNPs

The difference in bond lengths between the two sites plays a crucial role in determining the vibrational frequencies. At the tetrahedral (A) site, the oxygen-iron distance is 1.89 Å [29], leading to stronger covalent bonding, which in turn results in higher vibrational stretching frequencies. In contrast, the oxygen-iron distance at the octahedral [B] site is 1.99 Å, resulting in weaker bonding and therefore lower vibrational stretching frequencies. This contrast between the two sites is a key characteristic of spinel structures, where the arrangement of cations within the tetrahedral and octahedral voids leads to distinct vibrational behavior. The observation of two distinct interstitial stretching modes, represented by v_1 and v_2, provides direct confirmation of the spinel structure of $ZnFe_2O_4$ MNPs. The presence of these modes is a hallmark of the spinel lattice, where the metal ions are distributed among tetrahedral and octahedral sites in a specific geometric arrangement. The FTIR spectrum, with its clear distinction between these two vibrational modes, thus validates the spinel configuration of the material. This behavior is not limited to $ZnFe_2O_4$ but is a common feature of spinel ferrites, where subtle variations in bond length and coordination environment lead to complex vibrational patterns. These small structural differences can have significant implications for the material's properties, including its magnetic, electrical, and catalytic behavior. The complexity observed in the FTIR spectrum, arising from variations in

bond lengths and vibrational frequencies, mirrors the intricate interactions at the molecular level. This idea is reminiscent of Richard Feynman's famous remark that "the beauty of a flower may not be just in its color, but in the complexity it reveals." In the case of $ZnFe_2O_4$ and similar ferrites, the true beauty lies in the molecular interactions and the subtle yet profound differences in bonding that give rise to the observed physical properties [30].

Magnetic properties of $ZnFe_2O_4$ MNPs

The magnetic properties of $ZnFe_2O_4$ samples, including saturation magnetization (Ms), remanent magnetization (Mr), coercivity (HC), squareness ratio (Ms/Mr), and magneton number (nB), were thoroughly assessed using Pulse-Field Hysteresis Loop (PFHL) measurements (see **Figure 4**). The saturation magnetization, constrained by an applied field of 1000 Oe, was measured at 50 emu/g, while the remanent magnetization was 17 emu/g. These values reflect the disruption of exchange interactions at the nanoparticle surfaces, resulting in surface-canted spins [31].
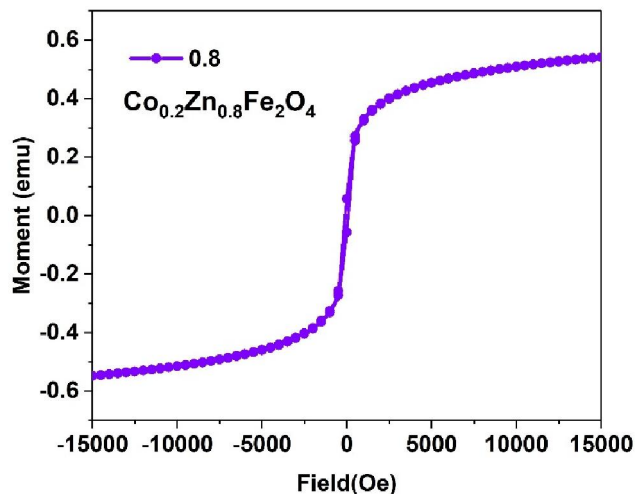

Figure 4 Hystersis loop of $ZnFe_2O_4$ MNPs

The coercivity (HC) of approximately 265 Oe was attributed to the influence of nanoscale size, which affects domain wall pinning and surface anisotropies, while the squareness ratio (Mr/Ms) of 0.36 indicated a mix of multi-domain and single-domain behavior in the material [32]. In the inverted spinel structure of $ZnFe_2O_4$, the magnetic moment of Co^{2+} ions at the octahedral [B] site was 2.0 µB, while the Fe^{3+} ions at the tetrahedral (A) and octahedral [B] sites effectively canceled each other's moments due to antiferromagnetic coupling. The magneton number (nB) per formula unit, calculated to be 1.77, indicated moderate A-B interaction, consistent with typical spinel ferrites [33, 34].

$$n_B = \frac{[M_S \times M_W]}{558\ 5} \qquad (4)$$

The observed surface anisotropy and spin canting, caused by reduced coordination and altered exchange interactions at the nanoparticle surface, led to a reduction in saturation magnetization and influenced the magnetic hysteresis behavior. These parameters, which align well with theoretical predictions, demonstrate the effects of particle size, surface structural characteristics, and synthesis conditions on the magnetic behavior of $ZnFe_2O_4$ nanoparticles.

DC-Electrical resistivity of $ZnFe_2O_4$ MNPs

Zinc ferrite, with a resistivity greater than 10^9 Ω·cm, is classified as a highly resistant material. As shown in **Figure 5**, the DC resistivity of $ZnFe_2O_4$ MNPs decreases as the temperature increases, indicating the material's conduction mechanism, which is attributed to the weak polaron hopping between Fe^{2+} and Fe^{3+} ions.
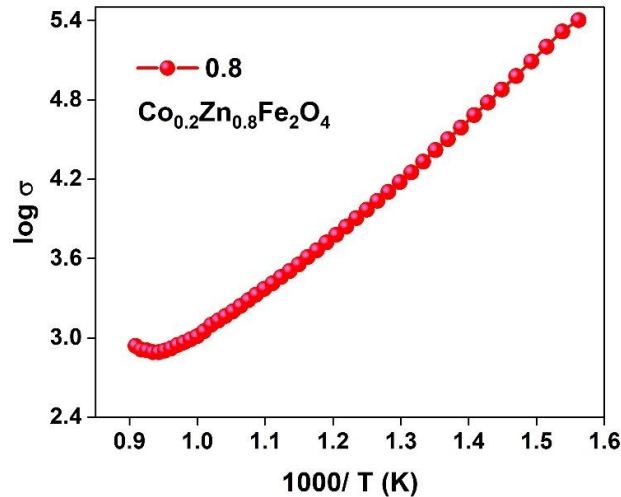
Figure 5 DC-electrical resistivity of $ZnFe_2O_4$ MNPs

This behavior confirms the semiconducting nature of $ZnFe_2O_4$ MNPs. For the characterization, the nanopowder was first compressed into a pellet with a diameter of 10 mm and a thickness of 2 mm using a KBr press. To ensure reliable electrical (Ohmic) contact, a thin layer of silver paste was applied to both sides of the pellet. The temperature-dependent DC resistivity was then measured in the range of 300–600 °C using a two-probe method. The DC electrical resistivity of spinel ferrites is influenced by factors such as the concentration of Fe^{2+} ions at octahedral [B] sites, grain size (G), sintering temperature, and porosity (P%). The electrical resistivity (ρ) was calculated using the Arrhenius relation, which describes the dependence of DC resistivity on temperature (T in K) [35];

$$\rho = \rho_0 \times \exp\left(\frac{\Delta E_a}{kT}\right) \tag{5}$$

In this equation, ρ_0 represents the temperature-independent resistivity, E_a is the activation energy, k is the Boltzmann constant, and T is the absolute temperature. The temperature-dependent mobility of charge carriers in ferrite materials is governed by the activation energy, which determines how resistivity changes with temperature was measured to be 3.11 eV. According to the Arrhenius relation, electrical resistivity decreases with increasing temperature, a behavior indicative of the material's semiconducting nature. In $ZnFe_2O_4$ MNPs, this decrease in resistivity occurs due to the enhanced drift mobility of charge carriers at elevated temperatures. As the temperature rises, more charge carriers gain sufficient energy to overcome potential barriers, resulting in increased mobility and lower resistivity. This behavior is described mathematically by the equation: $\mu = 1/ne\rho$ [36], where 'e' is the charge on the electron, " is the resistivity, and 'n' is the charge carrier concentration, which may be computed using the equation $n = Na\rho P/M_W$ [37], Where M_W stands for molecular weight, Na for Avogadro's number, ρ for sample density, and P for the amount of iron atoms in the oxide's chemical formula.

VI. CONCLUSION

The sol-gel auto-combustion method was successfully used to synthesize $ZnFe_2O_4$ magnetic nanoparticles (MNPs) with citric acid ($C_6H_8O_7$) serving as the fuel. The X-ray diffraction (XRD) pattern of the $ZnFe_2O_4$ MNPs confirmed the formation of a cubic spinel structure, belonging to the Fd3m-Oh7 space group. The measured lattice constant (a) for the synthesized MNPs was 8.384 ± 0.05 Å. Analysis of peak broadening using Debye-Scherrer's method revealed an average crystallite size (t) of 36 nm. The Fourier-transform infrared (FT-IR) spectra showed two prominent metal-oxide bands at approximately 541 cm⁻¹ (O-M Oct) and 409 cm⁻¹ (O-M Td), corresponding to the metal-oxygen bonds at the octahedral and tetrahedral sites, respectively, within the $ZnFe_2O_4$ structure. These bands, falling within the typical range of 370 to 600 cm⁻¹ for spinel ferrites, confirm the structural integrity of the synthesized material. Magnetic measurements indicated a saturation magnetization (Ms) of ~50 emu/g, a remanent magnetization (Mr) of ~17 emu/g,

and a magneton number (nB) of 1.77 emu/g. The activation energy (Ea) was determined to be 3.11 eV. Additionally, the DC electrical resistivity measurements, consistent with the Arrhenius equation, verified the semiconducting nature of the $ZnFe_2O_4$ MNPs.

VI. ACKNOWLEDGMENT

REFERENCES

[1] O. Bongomin, A. Yemane, B. Kembabazi, C. Malanda, M. Chikonkolo Mwape, N. Sheron Mpofu, D. Tigalana, Industry 4.0 disruption and its neologisms in major industrial sectors: A state of the art, Journal of Engineering, 2020 (2020) 8090521.

[2] P. Aithal, S. Aithal, Opportunities & Challenges for Green Technologies in 21st Century, Munich Personal RePEc Archive (MPRA), DOI (2016).

[3] S. Malik, K. Muhammad, Y. Waheed, Nanotechnology: A revolution in modern industry, Molecules, 28 (2023) 661.

[4] J.E. Lofgreen, G.A. Ozin, Controlling morphology and porosity to improve performance of molecularly imprinted sol–gel silica, Chemical Society Reviews, 43 (2014) 911-933.

[5] J. Smit, H. Wijn, Physical properties of ferrites, Advances in Electronics and Electron Physics, Elsevier1954, pp. 69-136.

[6] J. Mohapatra, M. Xing, J.P. Liu, Inductive thermal effect of ferrite magnetic nanoparticles, Materials, 12 (2019) 3208.

[7] M. Qin, Q. Shuai, G. Wu, B. Zheng, Z. Wang, H. Wu, Zinc ferrite composite material with controllable morphology and its applications, Materials Science and Engineering: B, 224 (2017) 125-138.

[8] N. Singh, A. Agarwal, Preparation, characterization, properties and applications of nano zinc ferrite, Materials Today: Proceedings, 5 (2018) 9148-9155.

[9] R. Ciriminna, A. Fidalgo, V. Pandarus, F. Beland, L.M. Ilharco, M. Pagliaro, The sol–gel route to advanced silica-based materials and recent applications, Chemical reviews, 113 (2013) 6592-6620.

[10] L.L. Hench, J.K. West, The sol-gel process, Chemical reviews, 90 (1990) 33-72.

[11] G.J. Owens, R.K. Singh, F. Foroutan, M. Alqaysi, C.-M. Han, C. Mahapatra, H.-W. Kim, J.C. Knowles, Sol–gel based materials for biomedical applications, Progress in materials science, 77 (2016) 1-79.

[12] S. Bid, S. Pradhan, Characterization of crystalline structure of ball-milled nano-Ni–Zn-ferrite by Rietveld method, Materials Chemistry and Physics, 84 (2004) 291-301.

[13] N. Deraz, A. Alarifi, Microstructure and magnetic studies of zinc ferrite nano-particles, International Journal of Electrochemical Science, 7 (2012) 6501-6511.

[14] K. Wu, J. Li, C. Zhang, Zinc ferrite based gas sensors: A review, Ceramics International, 45 (2019) 11143-11157.

[15] C. Chinnasamy, A. Narayanasamy, N. Ponpandian, K. Chattopadhyay, H. Guerault, J. Greneche, Magnetic properties of nanostructured ferrimagnetic zinc ferrite, Journal of Physics: Condensed Matter, 12 (2000) 7795.

[16] L. Kumar, P. Kumar, A. Narayan, M. Kar, Rietveld analysis of XRD patterns of different sizes of nanocrystalline cobalt ferrite, International Nano Letters, 3 (2013) 1-12.

[17] H. Zaki, S. Al-Heniti, T. Elmosalami, Structural, magnetic and dielectric studies of copper substituted nano-crystalline spinel magnesium zinc ferrite, Journal of Alloys and compounds, 633 (2015) 104-114.

[18] V. Senthil, J. Gajendiran, S.G. Raj, T. Shanmugavel, G.R. Kumar, C.P. Reddy, Study of structural and magnetic properties of cobalt ferrite (CoFe2O4) nanostructures, Chemical Physics Letters, 695 (2018) 19-23.

[19] H.K. Dubey, C. Verma, U. Rai, A. Kumar, P. Lahiri, Synthesis, characterization and properties of nickel based zinc ferrite nanoparticles, DOI (2019).

[20] T. Tatarchuk, M. Myslin, I. Mironyuk, M. Bououdina, A.T. Pędziwiatr, R. Gargula, B.F. Bogacz, P. Kurzydło, Synthesis, morphology, crystallite size and adsorption properties of nanostructured Mg–Zn ferrites with enhanced porous structure, Journal of Alloys and Compounds, 819 (2020) 152945.

[21] R. Ramadan, Zinc-doped hexaferrite exhibits altered physical properties in the presence of both Dy and Zn ions, Journal of Materials Science: Materials in Electronics, 35 (2024) 1402.

[22] A.N. Birgani, M. Niyaifar, A. Hasanpour, Study of cation distribution of spinel zinc nano-ferrite by X-ray, Journal of Magnetism and Magnetic Materials, 374 (2015) 179-181.

[23] S.R. Patade, D.D. Andhare, S.B. Somvanshi, P.B. Kharat, S.D. More, K.M. Jadhav, Preparation and characterisations of magnetic nanofluid of zinc ferrite for hyperthermia, Nanomaterials and Energy, DOI (2020) 1-6.

[24] M.C. Varma, G. Choudary, A.M. Kumar, K. Rao, Estimating the Cation Distributions in Ni0. 65− xZn0. 35CoxFe2O4 Ferrites Using X-Ray, FT-IR, and Magnetization Measurements, Physics Research International, 2014 (2014) 579745.

[25] M. Raghasudha, D. Ravinder, P. Veerasomaiah, Characterization of chromium substituted cobalt nano ferrites synthesized by citrate-gel auto combustion method, DOI (2013).

[26] P.A. Vinosha, L.A. Mely, J.E. Jeronsia, F.H. Monica, K. Raja, S.J. Das, Study of Structural, optical, dielectric and magnetic properties of zinc ferrite synthesized by co-precipitation, Nano Hybrids and Composites, 17 (2017) 1-9.

[27] M. Deepty, C. Srinivas, E.R. Kumar, N.K. Mohan, C. Prajapat, T.C. Rao, S.S. Meena, A.K. Verma, D. Sastry, XRD, EDX, FTIR and ESR spectroscopic studies of co-precipitated Mn–substituted Zn–ferrite nanoparticles, Ceramics International, 45 (2019) 8037-8044.

[28] J.P. Singh, G. Dixit, R. Srivastava, P. Negi, H. Agrawal, R. Kumar, HRTEM and FTIR investigation of nanosized zinc ferrite irradiated with 100 MeV oxygen ions, Spectrochimica Acta Part A: Molecular and Biomolecular Spectroscopy, 107 (2013) 326-333.

[29] C. Uebing, Two-dimensional transition metal compounds with carbon, nitrogen and oxygen on BCC (100) metal and alloy surfaces, Progress in solid state chemistry, 26 (1998) 155-240.

[30] H. Kumar, J.P. Singh, R. Srivastava, P. Negi, H. Agrawal, K. Asokan, FTIR and electrical study of dysprosium doped cobalt ferrite nanoparticles, Journal of Nanoscience, 2014 (2014) 862415.

[31] A. Spaggiari, D. Castagnetti, N. Golinelli, E. Dragoni, G. Scirè Mammano, Smart materials: Properties, design and mechatronic applications, Proceedings of the institution of mechanical engineers, part l: journal of materials: design and applications, 233 (2019) 734-762.

[32] N. Nuñez, M. Rainieri Andersen, E. Lima Jr, H.E. Troiani, D. Tobia, R.D. Zysler, E.L. Winkler, Desarrollo de nanocompuestobifuncional para aplicacionesenhipertermiamagnética y sensible a la radaciónionizante, DOI (2023).

[33] A.V. Humbe, A.C. Nawle, A. Shinde, K. Jadhav, Impact of Jahn Teller ion on magnetic and semiconducting behaviour of Ni-Zn spinel ferrite synthesized by nitrate-citrate route, Journal of Alloys and Compounds, 691 (2017) 343-354.

[34] A.E. Nowacka, Divalent metal organic frameworks as heterogeneous oxidation catalysts, 2019.

[35] M.V. Shisode, A.V. Humbe, P.B. Kharat, K. Jadhav, Influence of Ba 2+ on opto-electric properties of nanocrystalline BiFeO 3 multiferroic, Journal of Electronic Materials, 48 (2019) 358-367.

[36] G.J. Snyder, A.H. Snyder, M. Wood, R. Gurunathan, B.H. Snyder, C. Niu, Weighted Mobility, Advanced Materials, DOI (2020) 2001537.

[37] S. Singh, S. Katyal, N. Goswami, Dielectric and electrical study of zinc copper ferrite nanoparticles prepared by exploding wire technique, Applied Physics A, 125 (2019) 638

Copyright to IJARSCT
www.ijarsct.co.in

DOI: 10.48175/568

ISSN
2581-9429
IJARSCT

298